Diamond optomechanical crystals

DIAMOND OPTOMECHANICAL CRYSTALS

Michael J. Burek[a], Justin D. Cohen[b], Seán M. Meenehan[b], Thibaud Ruelle[a,c], Srujan Meesala[a], Jake Rochman[a,d], Haig Atikian[a], Matthew Markham[e], Daniel J. Twitchen[e], Mikhail D. Lukin[f], Oskar Painter[b], and Marko Lončar[a,†]

[a.] John A. Paulson School of Engineering and Applied Sciences, Harvard University, 29 Oxford Street, Cambridge, MA 02138, USA

[b.] Kavli Nanoscience Institute, Institute for Quantum Information and Matter and Thomas J. Watson, Sr., Laboratory of Applied Physics, California Institute of Technology, Pasadena, CA 91125, USA

[c.] École Polytechnique Fédérale de Lausanne (EPFL), CH-1015 Lausanne, Switzerland

[d.] University of Waterloo, 200 University Avenue West, Waterloo, ON, N2L 3G1, Canada

[e.] Element Six Innovation, Fermi Avenue, Harwell Oxford, Didcot, Oxfordshire OX110QR, UK

[f.] Department of Physics, Harvard University, 17 Oxford Street, Cambridge, MA 02138, USA

[†] Corresponding author contact: E-mail: loncar@seas.harvard.edu. Tel: (617) 495-579. Fax: (617) 496-6404.

Cavity-optomechanical systems[1] realized in single-crystal diamond are poised to benefit from its extraordinary material properties, including low mechanical dissipation and wide optical transparency window. Diamond is also rich in optically active defects, such as the nitrogen-vacancy (NV) center, which behave as atom-like systems in the solid state[2]. Predictions and observations of coherent coupling of the NV electronic spin to phonons via lattice strain[3-7] has motivated the development of diamond nanomechanical devices aimed at realization of hybrid quantum systems[8,9], in which phonons provide an interface with diamond spins. In this work, we demonstrate a device platform to enable such applications: *diamond optomechanical crystals* (OMCs), where the co-localization of ~ 200 THz photons and ~ 6 GHz phonons in a quasi-periodic diamond nanostructure leads to coupling of an optical cavity field to a mechanical mode via the radiation pressure of light. In contrast to other material systems, diamond OMCs operating in the resolved sideband regime possess large intracavity photon capacity (> 10^5) and sufficient optomechanical coupling rate to exceed a cooperativity of ~ 1 at room temperature and realize large amplitude optomechanical self-oscillations[10]. Strain-mediated coupling of the high frequency (~ GHz) mechanical modes of these devices to the electronic and spin levels of diamond color centers has the potential to reach the strong spin-phonon coupling regime, and enable a coherent interface with diamond qubits for applications in quantum-nonlinear optomechanics.

Optomechanical crystals (OMCs), first demonstrated in silicon[1], and later in other materials like silicon nitride[11,12] and gallium arsenide[13], have emerged as a fruitful optomechanics platform, wherein radiation pressure effects provide exquisitely sensitive optical control of mechanical vibrations. Such systems have enabled demonstrations of quantum ground state cooling[14], optomechanically induced transparency[15], squeezed light[16], and wavelength conversion[17]. Highly coherent photon-phonon interactions in OMCs is the direct result of the ability to engineer a large single-photon optomechanical coupling rate (g_o), while retaining sufficiently small optical (κ) and intrinsic mechanical (γ_i) dissipation

rates. Similar structures realized in single-crystal diamond – which features a unique combination of superior mechanical, thermal, and optical properties[18] – are expected to exhibit pronounced optomechanical interactions, quantified by the cooperativity parameter $C = 4n_c g_o^2 / \kappa \gamma_i$ (where n_c is the intracavity photon number). Specifically, diamond's wide bandgap (~ 5.5 eV) precludes two- or multi-photon absorption over a wide wavelength range (from visible to infrared). This, combined with its high thermal conductivity and small thermal expansion, enables monolithic diamond optical cavities that can withstand significant optical power densities, while avoiding degradation in optical linewidth or drifts in resonance wavelength due to thermal lensing. Diamond's large intracavity photon capacity can thus result in large cooperativities necessary for either strong mechanical driving or effective laser cooling[14]. Moreover, diamond is among the stiffest materials known and possess extremely low thermoelastic mechanical damping, with recently demonstrated monolithic diamond cantilevers exhibiting mechanical Q-factors in excess of 10^6 at room temperature[19]. In what follows, we make use of these features to demonstrate OMCs in single-crystal diamond with unique performance. Our diamond OMCs support a $\omega_m/2\pi \sim 6$ GHz mechanical cavity coupled to a co-resonant photon field at $\omega_o/2\pi \sim 200$ THz, with vacuum optomechanical coupling rate of $g_o \sim 100$ kHz. With an optical linewidth of $\kappa/2\pi \sim 2.5$ GHz, this diamond OMC system operates in the so-called resolved sideband regime ($\omega_m/\kappa > 1$), necessary for efficient radiation-pressure driven dynamic backaction. This enables our diamond OMCs to be optically driven to $C > 1$ at room temperature, highlighted by the observation of "phonon lasing" in our structures[10].

Diamond OMCs consist of a one dimensional nanobeam photonic crystal cavity fabricated in single-crystal diamond[20] using previously developed 'angled-etching' techniques[21]. The nanobeam cavity is based on a triangular cross-section diamond waveguide perforated with a periodic lattice of elliptically shaped air holes. A photonic bandstructure of one unit cell in this waveguide (Figure 1 (a)), shown in Figure 1 (b), includes both transverse electric (TE-like, solid black lines) and transverse magnetic (TM-

like, dashed blue lines) guided modes. In this work, we focus on TE-like modes near the X-point frequency of $\omega_o/2\pi \sim 200$ THz ($\lambda \sim 1550$ nm), since they can lead to the realization of very high Q-factor optical cavities[20]. Importantly, our photonic crystal waveguide also supports acoustic guided modes that are spatially overlapped with optical modes, and can couple to them via radiation pressure. The corresponding mechanical bandstructure (Figure 1 (c)) reveals a rich library of guided acoustic modes in the few to 10 GHz frequency range. The guided modes, categorized by even (solid black lines) and odd (dashed blue lines) vector symmetries about the *y*-axis, again yield symmetry based quasi-bandgaps. Following OMC design rules[22,23], we identified the guided mode derived from the Γ-point of the fourth *y*-symmetric band (frequency of $\omega_m/2\pi \sim 6$ GHz) – referred hereafter as the "flapping" acoustic mode (Figure 1 (d)) – as the mechanical mode of interest for large optomechanical coupling. While other mechanical guided modes suitable for large optomechanical coupling exist (see *Supplementary Information*), we focus on this particular mode due to a large acoustic quasi-bandgap below its native band (indicated by the shaded pink region in Figure 1 (c)).

To realize a diamond OMC cavity from the aforementioned OMC waveguide, the lattice of air holes is chirped[22] (Figure 1(e) and (f)) such as to transition from a "mirror" region formed by the base unit cell in Figure 1 (a) to a "defect" cell. The defect cell dimensions are selected to simultaneously raise and lower the frequencies of the target optical and mechanical modes, respectively, into their respective quasi-bandgaps. Gradually reducing the unit cell lattice constant while also decreasing the air hole aspect ratio (h_w/h_h) achieves the necessary band edge tuning (see insets of Figure 1 (b) and (c)). An optimized design (see *Supplementary Information*) was determined via numerical optimization methods, based upon FEM simulations (COMSOL) to calculate the optical (ω_o) and mechanical (ω_m) cavity resonance frequencies, the optical Q-factor (Q_o), and g_o. Both moving boundary ($g_{o,MB}$) and photo-elastic ($g_{o,PE}$) contributions to the single-photon optomechanical coupling rate were considered (see *Supplementary Information*), with the calculation of $g_{o,PE}$ using the following photoelastic coefficients of

diamond[24]: (p_{11}, p_{12}, p_{44}) = (-0.25, 0.043, -0.172). Normalized electric field (E_y) and mechanical displacement profiles (*xz*-plane) of the final optimized diamond OMC design are shown in Figure 1 (e) and (f), respectively. The optimized design – which assumes x-axis orientation aligned with the in plane [110] crystallographic direction – has an optical resonance at $\omega_o/2\pi$ = 195 THz (λ_o = 1539 nm), radiation-limited optical *Q*-factor of 1.02 x 10^6, mode volume of $0.75(\lambda/n)^3$, mechanical resonance at $\omega_m/2\pi$ = 6.11 GHz, effective mass of 607 fg, and zero-point motion of x_{zpf} = 3.1 fm. The final coupling rate for this design was go/2π = 116 kHz, and included a moving boundary and photo-elastic contribution of $g_{o,MB}/2\pi$ = 53 kHz and $g_{o,PE}/2\pi$ = 63 kHz, respectively.

As previously mentioned, fabrication of diamond OMCs utilized angled-etching techniques[20,21] (Figure 2 (a) and described in *Methods*), which employ anisotropic oxygen-based plasma etching at an oblique angle to the substrate surface resulting in suspended structures with triangular cross-section. The final fabricated structures, displayed in Figure 2 (b) to (d), reveal excellent reproduction of the intended design. A unique consideration of angled-etched structures is their triangular cross-section symmetry (see *Supplementary Information* for further discussion). A high-resolution SEM image shown in Figure 2 (e) reveals a fabricated diamond OMC (oriented upside down), with insets displaying a tilted cross-sectional view.

An optical transmission spectrum – obtained with the characterization set up shown in Figure 3 (a) and described in *Methods* – of a representative diamond OMC is shown in Figure 3 (b). A Lorentzian fit to the optical cavity resonance gives a measured total and intrinsic optical Q-factor of 7.85 x 10^4 and 1.20 x 10^5, respectively. The corresponding total cavity decay rate, fiber taper coupling rate, and intrinsic optical decay rate are $\kappa/2\pi$ = 2.49 GHz, $\kappa_e/2\pi$ = 0.86 GHz, and $\kappa_i/2\pi$ = 1.63 GHz, respectively. With the expected diamond OMC mechanical resonance at ~ 6 GHz, the optical cavity decay rate places the optomechanical system into the resolved sideband regime, with $\omega_m/\kappa \sim 2.42$. In this regime, while the input laser is either red- or blue-detuned from the optical cavity position by a mechanical frequency (Δ =

($\omega_o - \omega_l$) = ± ω_m), mechanical motion of the acoustic mode modulates transmitted light, giving rise to a sideband of the input laser resonant with the optical cavity. The other first-order motional sideband (which is not resonant with the optical cavity) is suppressed in this scenario. As a result, mechanical motion produces an intensity modulation in the radio frequency (RF) power spectrum of the photodetector. The RF spectrum of thermally excited mechanical mode at room temperature (i.e., thermal Brownian motion) is shown in Figure 3 (c), and reveals a Lorentzian mechanical resonance of the diamond OMC centered at $\omega_m/2\pi$ = 6.023 GHz with a Q_m ~ 3800. This corresponds to a $f \cdot Q$ product of ~ 2.3 x 10^{13} Hz, which is among the highest demonstrated for either a bulk or small-scale diamond mechanical oscillator at room temperature[6,25].

With the laser detuning conditions described above, optomechanical backaction causes an additional damping rate in the resolved-sideband limit[26] of $\gamma_{OM} = \pm 4 n_c g_o^2 / \kappa$ for $\Delta = \pm \omega_m$, where n_c is calculated from the input laser power (P_i) by the relation $n_c = P_i \left(\kappa_e / 2\hbar\omega_l \left((\kappa/2)^2 + \Delta^2 \right) \right)$. Figure 3 (d) plots the measured mechanical linewidth taken with both red- and blue-sideband laser detuning as a function of input power all the way up to the maximum output of the laser (n_c ~ 31,000 photons). The effects of backaction are clearly visible, with the laser red detuned ($\Delta = +\omega_m$; γ_{red}) resulting in damping and the laser blue detuned ($\Delta = -\omega_m$; γ_{blue}) giving rise to anti-damping of motion. From the mean value extracted from γ_{red} and γ_{blue} data points the estimated intrinsic mechanical linewidth is $\gamma_i/2\pi$ = 1.63 +/- 0.01 MHz. The optomechanical coupling rate, calculated as $\gamma_{OM} = \gamma_i - \gamma_{blue}$, is plotted versus n_c in Figure 3 (e), where a linear fit yields $g_o/2\pi$ = 101 kHz. This estimate differs only slightly from our design, which we attribute to uncertainty in the photo-elastic constants of diamond at telecom frequencies, as well as fabrication imperfections. To verify our estimate of γ_i and g_o, the laser frequency was first blue-detuned and then swept between $\Delta = -\omega_m \pm \kappa$ while maintaining a constant n_c, yielding the detuning dependence of the optically amplified mechanical damping rate (Figure 3 (f)) and the optical spring shifted mechanical frequency (Figure 3 (g)). Fits to backaction amplification and optical spring curves,

following Eq. (6) and Eq. (7) of Ref [26], yield a second estimate of $\gamma_i/2\pi$ = 1.60 MHz and $g_o/2\pi$ = 102 kHz, in close agreement with the previously stated values. A static thermal softening of the diamond material likely causes the slight deviation of data in Figure 3(g) from a pure radiation-pressure driven back-action optical spring effect. As the detuning approaches zero and the laser enters the cavity resonance, the diamond OMC temperature is raised due to non-negligible linear optical absorption, resulting in thermal expansion and a reduction in Young's modulus[27].

To drive γ_{OM} beyond the level reached with the tunable laser output alone, an erbium doped fiber amplifier (EDFA) was inserted after the pump laser to enable large n_c. Figure 4 (a) plots the mechanical linewidth at high input powers, with the laser blue-detuned by a mechanical frequency, while Figure 4 (b) plots corresponding cooperativity values, $C = \gamma_{OM}/\gamma_i$, calculated with the previously determined γ_i. At an input power corresponding to approximately $n_c \sim 10^5$, the diamond OMC reached C ~ 1, exciting the mechanical cavity into large amplitude optomechanical self-oscillations, so-called "phonon lasing"[10]. Mechanical spectra of the diamond OMC taken below, at, and above this phonon lasing threshold (shown in Figure 4 (c)) show an over 60 dB increase in peak amplitude, with a threshold input power of $n_{c,thr} \sim 10^5$.

For a second diamond OMC device, a similar measurement scheme was carried out, with n_c increased beyond the observed phonon lasing threshold. The relevant parameters experimentally extracted for this device (λ_o Q_i, $\kappa/2\pi$, $\omega_m/2\pi$, $\gamma_i/2\pi$, $g_o/2\pi$) = (1544.5 nm, 1.54 x 10^5, 2.62 GHz, 6.13 GHz, 1.74 MHz, 106 kHz), yielded a $n_{c,thr} > 9.0 \times 10^4$ (as represented by the vertical dashed blue line in Figure 4 (e)). By increasing n_c beyond this value with the laser tuned to the red motional sideband, a final cooperativity value of $C \sim 1.8$ was reached at an optical cavity occupation of $n_c \sim 1.7 \times 10^5$ photons (see inset). Beyond this input power level, thermal-optic bistability shifts (likely originating from surface absorption) made it difficult to achieve precise laser detuning equal to the mechanical frequency, resulting in measured mechanical linewidths that deviate from the linear fit of the data. This established

a second maximum power threshold ($n_{c,max}$), indicated by the vertical dashed grey line. In relation to previous reported limits, diamond OMCs have an intracavity photon capacity over twice as large as OMC structures realized in silicon nitride[11,12].

In summary, we have demonstrated resolved sideband cavity-optomechanics in single-crystal diamond, where optomechanical coupling via radiation pressure was sufficient to exceed a cooperativity of ~ 1 for an intracavity photon population on the order of 10^5. Present devices also offer a promising platform for reaching much larger cooperativities when, for instance, operated at cryogenic temperatures, where mechanical Q-factors of diamond resonators have been shown to improve significantly[19]. Moreover, incorporating diamond color centers with monolithic OMCs is an interesting route to applications in quantum-nonlinear optomechanics. Diamond is rich in optically active defects (color centers), such as the nitrogen-vacancy (NV) center, which behave as atom-like systems in the solid state[2]. Recent experiments[3-7] exploring coherent coupling of the NV electronic spin to phonons in mechanical resonators via lattice strain have demonstrated manipulation of the NV spin state at large driven mechanical amplitudes, but remain far below the strong spin-phonon coupling regime. One way to boost this interaction would be to engineer truly nanoscale resonators, with feature sizes of a few hundred nm, and with frequencies in the hundreds of MHz to few GHz range – such mechanical modes would provide a large change in local strain per phonon[7]. The localized phononic modes of OMCs not only satisfy these requirements[28], but also are conveniently actuated and transduced with optical fields in the well-established telecom wavelength range. Diamond OMCs with coupled color centers may ultimately be used to map non-classical spin qubit states as well as quantum states of light onto phonons and vice-versa[29], and will enable fundamentally new ways to prepare, control, and read out the quantum states of diamond qubits. Lastly, individual diamond OMCs integrated into larger arrays coupled through phononic waveguides[30] could enable long-range spin-spin interactions mediated by phonons[8].

We note that, parallel to this work, Mitchell *et al.* have demonstrated cavity optomechanics in single

crystal diamond microdisks[31].

This work was supported in part by the ONR Quantum Optomechanics MURI (Award No. N00014-15-1-2761), AFOSR Quantum Memories MURI (grant FA9550-12-1-0025), DARPA QuINESS program, NSF QOP (grant PHY-0969816), and NSF CUA (grant PHY-1125846), the Institute for Quantum Information and Matter, an NSF Physics Frontiers Center with support of the Gordon and Betty Moore Foundation, and the Kavli Nanoscience Institute at Caltech. M.J. Burek and H.A. Atikian were supported in part by the Harvard Quantum Optics Center (HQOC). T. Ruelle was supported in part from the Fondation Zdenek and Michaela Bakala. This work was performed in part at the Center for Nanoscale Systems (CNS), a member of the National Nanotechnology Infrastructure Network (NNIN), which is supported by the National Science Foundation under NSF award no. ECS-0335765. CNS is part of Harvard University.

METHODS

Angled-etching nanofabrication

Single-crystal diamond substrates were grown using microwave-assisted chemical vapor deposition such that they contained a low nitrogen concertation (< 5 ppb) and were orientated with a (100) major face and <110> edges. Diamond substrates were subsequently polished to a surface roughness < 5 nm RMS (performed by Delware Diamond Knives), followed by cleaning in a boiling mixture consisting of equal parts concentrated sulfuric acid, nitric acid, and perchloric acid. A pre-fabrication surface preparation (performed in a UNAXIS Shuttleline inductively coupled plasma-reactive ion etcher (ICP-RIE)) included a 30 minute etch with the following parameters: 400 W ICP power, 250 RF power, 25 sccm Ar flow rate, 40 sccm Cl_2 flow rate, and 8 mTorr chamber pressure, followed by a second 30 minute etch with the following parameters: 700 W ICP power, 100 RF power, 50 sccm O_2 flow rate, and 10 mTorr chamber pressure. The purpose of this pre-fabrication step was to reduce the surface roughness of the diamond substrate to < 1 nm RMS and remove several microns from the top of the diamond substrate which is likely strained due to previous mechanical polishing.

Fabrication of diamond OMCs utilized a silica etch mask, patterned on the diamond substrates using hydrogen silsesquioxane (HSQ, FOX®-16 from Dow Corning) negative resist and electron beam lithography. Exposure of the etch mask ensured alignment of the x-axis of the diamond optomechanical crystal with the [110] in plane crystallographic direction, confirmed prior to fabrication by electron backscattered diffraction measurements. Exposed HSQ was developed in tetramethylammonium hydroxide (TMAH, 25% diluted solution). A conventional top down anisotropic plasma etch (also performed in the UNAXIS Shuttleline RIE-ICP) with the following parameters: 700 W ICP power, 100 RF power, 50 sccm O_2 flow rate, 2 sccm Cl_2 flow rate, and 10 mTorr chamber pressure, was done to first transfer the silica etch mask pattern into the diamond. The diamond was etched to a depth of ~ 1000 nm. Following this, the angled-etching step was performed to realize the final free-standing diamond OMCs. Angled-etching was achieved using the same RIE-ICP parameters as the initial top down etch, but included housing the sample inside a specifically designed aluminum Faraday cage[20,21] to direct the plasma ions to the substrate surface at the intended angle. Following the oxygen-based plasma etching, the remaining etch mask was removed in concentrated hydrofluoric acid. Diamond OMCs were cleaned in piranha solution prior to optical and mechanical mode spectroscopy.

To investigate the backside of the fabricated diamond OMCs, we used a stamping technique to transfer angled-etch diamond nanobeams from their bulk diamond substrate, onto a smooth silver thin film supported by a silicon wafer. While this technique is ultimately destructive, it ensured that many diamond nanobeams are simultaneously removed and transferred to a conductive substrate, with most ending up on their backside such that the angled-etched surfaces are revealed.

Optical and mechanical spectroscopy

Characterization of fabricated diamond OMCs, performed under ambient conditions, used a dimpled fiber taper (set up illustrated in Figure 3 (a)) to evanescently couple to the device under test (as illustrated by the optical micrograph included as the inset). A tunable telecom laser diode (New Focus Velocity TLB-6328, C-band) was used locate the optical cavity resonance. A small percentage of the

input laser sent to a wavelength meter (λ-meter) via a 90:10 coupler (BS) enabled a stabilized laser frequency position. For measurements displayed in Figure 3, the laser was coupled directly to a variable optical attenuator (VOA), while high power measurements displayed in Figure 4 used an erbium doped fiber amplifier (EDFA) to boost the input power. A tunable filter placed after the EDFA removed the majority of amplified spontaneous emission (ASE) from the transmitted signal. After the VOA, the laser light was first sent through a fiber polarization controller (FPC) to maximize coupling with the device under test, and then into the dimpled fiber taper. The dimpled fiber taper position with respect to the device under test was precisely controlled via motorized stages with 50 nm encoder resolution. Optical scans of the device under test were initially collected with the dimpled fiber taper hovering above the device, to evaluate the optical cavity parameters under weak fiber coupling. For final measurements, the dimpled fiber was placed in direct contact with the device under test, in a position such as to maximize coupling while minimizing parasitic losses due to dielectric loading of the cavity by the silica fiber taper. A 2 x 2 fiber switch (SW2) was used to control the direction of light through the device region and allow for precise calibration of insertion and bidirectional coupling losses. After passing the device, the transmitted signal was switched between a low speed and high speed path, in order to collect the optical cavity spectrum and mechanical cavity spectrum respectively. In the high speed path, transmitted laser light is optically amplified by a second EDFA and then detected by a high-speed photodetector (D1, New Focus 1554-B, 12 GHz bandwidth). The high speed detector is connected to a real-time spectrum analyzer (RSA) to measure photocurrent electronic power spectrum and monitor the mechanical cavity response. In the low speed path, transmitted laser light is sent to a nanosecond photodetector (D2) used to measure the DC transmission response of the optical cavity.

REFERENCES

1 Eichenfield, M., Chan, J., Camacho, R. M., Vahala, K. J. & Painter, O. Optomechanical crystals. *Nature* **462**, 78-82 (2009).

2 Aharonovich, I. *et al.* Diamond-based single-photon emitters. *Reports on Progress in Physics* **74**, 076501 (2011).

3 Ovartchaiyapong, P., Lee, K. W., Myers, B. A. & Jayich, A. C. B. Dynamic strain-mediated coupling of a single diamond spin to a mechanical resonator. *Nat Commun* **5** (2014).

4 MacQuarrie, E. R. *et al.* Coherent control of a nitrogen-vacancy center spin ensemble with a diamond mechanical resonator. *Optica* **2**, 233-238, doi:10.1364/OPTICA.2.000233 (2015).

5 Teissier, J., Barfuss, A., Appel, P., Neu, E. & Maletinsky, P. Strain Coupling of a Nitrogen-Vacancy Center Spin to a Diamond Mechanical Oscillator. *Physical Review Letters* **113**, 020503 (2014).

6 MacQuarrie, E. R., Gosavi, T. A., Jungwirth, N. R., Bhave, S. A. & Fuchs, G. D. Mechanical Spin Control of Nitrogen-Vacancy Centers in Diamond. *Physical Review Letters* **111**, 227602 (2013).

7 Meesala, S. *et al.* Enhanced strain coupling of nitrogen vacancy spins to nanoscale diamond cantilevers. *arXiv:1511.01548* (2015).

8 Stannigel, K., Rabl, P., Sørensen, A. S., Zoller, P. & Lukin, M. D. Optomechanical Transducers for Long-Distance Quantum Communication. *Physical Review Letters* **105**, 220501 (2010).

9 Wallquist, M., Hammerer, K., Rabl, P., Lukin, M. & Zoller, P. Hybrid quantum devices and quantum engineering. *Physica Scripta* **2009**, 014001 (2009).

10 Grudinin, I. S., Lee, H., Painter, O. & Vahala, K. J. Phonon Laser Action in a Tunable Two-Level System. *Physical Review Letters* **104**, 083901 (2010).

11 Davanço, M., Ates, S., Liu, Y. & Srinivasan, K. Si 3 N 4 optomechanical crystals in the resolved-sideband regime. *Applied Physics Letters* **104**, 041101 (2014).

12 Grutter, K. E., Davanco, M. & Srinivasan, K. Si3N4 Nanobeam Optomechanical Crystals. *Selected Topics in Quantum Electronics, IEEE Journal of* **21**, 1-11 (2015).

13 Balram, K. C., Davanço, M., Lim, J. Y., Song, J. D. & Srinivasan, K. Moving boundary and photoelastic coupling in GaAs optomechanical resonators. *Optica* **1**, 414-420 (2014).

14 Chan, J. *et al.* Laser cooling of a nanomechanical oscillator into its quantum ground state. *Nature* **478**, 89-92 (2011).

15 Safavi-Naeini, A. H. *et al.* Electromagnetically induced transparency and slow light with optomechanics. *Nature* **472**, 69-73 (2011).

16 Safavi-Naeini, A. H. *et al.* Squeezed light from a silicon micromechanical resonator. *Nature* **500**, 185-189 (2013).

17 Hill, J. T., Safavi-Naeini, A. H., Chan, J. & Painter, O. Coherent optical wavelength conversion via cavity optomechanics. *Nat Commun* **3**, 1196 (2012).

18 Coe, S. E. & Sussmann, R. S. Optical, thermal and mechanical properties of CVD diamond. *Diamond and Related Materials* **9**, 1726-1729 (2000).

19 Tao, Y., Boss, J. M., Moores, B. A. & Degen, C. L. Single-crystal diamond nanomechanical resonators with quality factors exceeding one million. *Nat Commun* **5** (2014).

20 Burek, M. J. *et al.* High quality-factor optical nanocavities in bulk single-crystal diamond. *Nat Commun* **5** (2014).

21 Burek, M. J. *et al.* Free-Standing Mechanical and Photonic Nanostructures in Single-Crystal Diamond. *Nano Letters* **12**, 6084-6089 (2012).
22 Chan, J., Safavi-Naeini, A. H., Hill, J. T., Meenehan, S. & Painter, O. Optimized optomechanical crystal cavity with acoustic radiation shield. *Applied Physics Letters* **101**, 081115 (2012).
23 Eichenfield, M., Chan, J., Safavi-Naeini, A. H., Vahala, K. J. & Painter, O. Modeling dispersive coupling and losses of localized optical andmechanical modes in optomechanicalcrystals. *Opt. Express* **17**, 20078-20098 (2009).
24 Lang, A. R. The strain-optical constants of diamond: A brief history of measurements. *Diamond and Related Materials* **18**, 1-5 (2009).
25 Rath, P., Ummethala, S., Nebel, C. & Pernice, W. H. P. Diamond as a material for monolithically integrated optical and optomechanical devices. *physica status solidi (a)* **212**, 2385-2399 (2015).
26 Safavi-Naeini, A. H. *et al.* Laser noise in cavity-optomechanical cooling and thermometry. *New Journal of Physics* **15**, 035007 (2013).
27 Zouboulis, E. S., Grimsditch, M., Ramdas, A. K. & Rodriguez, S. Temperature dependence of the elastic moduli of diamond: A Brillouin-scattering study. *Physical Review B* **57**, 2889-2896 (1998).
28 Kipfstuhl, L., Guldner, F., Riedrich-Möller, J. & Becher, C. Modeling of optomechanical coupling in a phoxonic crystal cavity in diamond. *Opt. Express* **22**, 12410-12423 (2014).
29 Bennett, S. D. *et al.* Phonon-Induced Spin-Spin Interactions in Diamond Nanostructures: Application to Spin Squeezing. *Physical Review Letters* **110**, 156402 (2013).
30 Fang, K., Matheny, M. H., Luan, X. & Painter, O. Phonon routing in integrated optomechanical cavity-waveguide systems. *arXiv:1508.05138* (2015).
31 Private communication with P. Barclay. (2015)

FIGURES

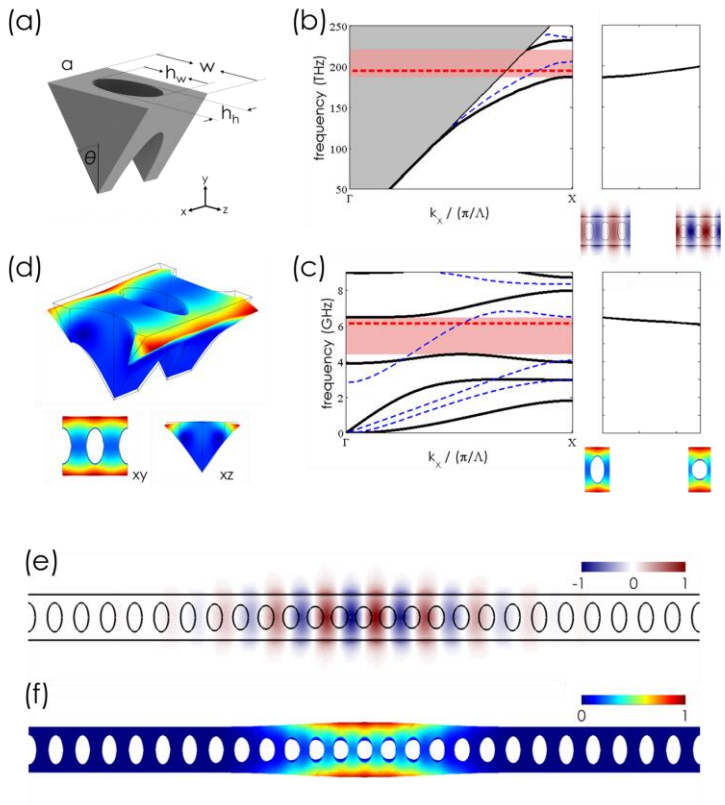

Figure 1 | Diamond optomechanical crystal optimized design. (a) Solid model representation of the triangular cross-section diamond unit cell as fabricated by angled-etching. The unit cell is parameterized by the etch angle (θ), width (w), lattice constant (a), and major and minor elliptical air hole diameters (h_w, h_h). Corresponding **(b)** optical and **(c)** mechanical band structures of a nominal unit cell with $\theta = 35^o$ and (a, w, h_w, h_h) = (540, 930, 590, 295) nm. In **(b)**, the grey shaded region indicates the continuum of radiation and leaky modes that exist above the light line for the structure. Below the light line, supported transverse electric (TE-like) and transverse magnetic (TM-like) guided modes are indicted by solid black and dashed blue lines, respectively. In **(c)**, mechanical guided modes shown are for propagation along the x-axis, with y-symmetric and y-antisymmetric vector symmetries again indicated by solid black and dashed blue lines, respectively. Mechanical simulations assume guided mode propagation is oriented with the in plane [110] crystallographic direction, with the z-axis is oriented with [001]. The red shaded regions in **(b)** and **(c)**, highlight the optical and mechanical symmetry bandgaps of interest, respectively. **(d)** Three-dimensional mechanical displacement profile of the "flapping" guided mode originating from the Γ-point of the fourth band with y-symmetric vector symmetry – identified as the mechanical mode which yields large displacement and strain overlap with the optical guided mode originating from the X-point of the first (dielectric) TE-like band. Right panels in **(b)** and **(c)** show the tuning of the X-point optical and Γ-point mechanical modes of interest as the unit cell is transitioned smoothly from the nominal unit cell to a defect cell with reduced lattice constant and decreased y-axis air hole eccentricity, specifically (a_{defect}, $h_{w,defect}$, $h_{h,defect}$) = (481, 430, 328) nm. Normalized **(e)** optical E_y field and **(f)** mechanical displacement profile of the localized optical and mechanical modes of the optimized diamond optomechanical crystal design. The eigenfrequencies of these localized optical and mechanical modes are indicated on the respective bandstructures in **(b)** and **(c)** by dashed red lines.

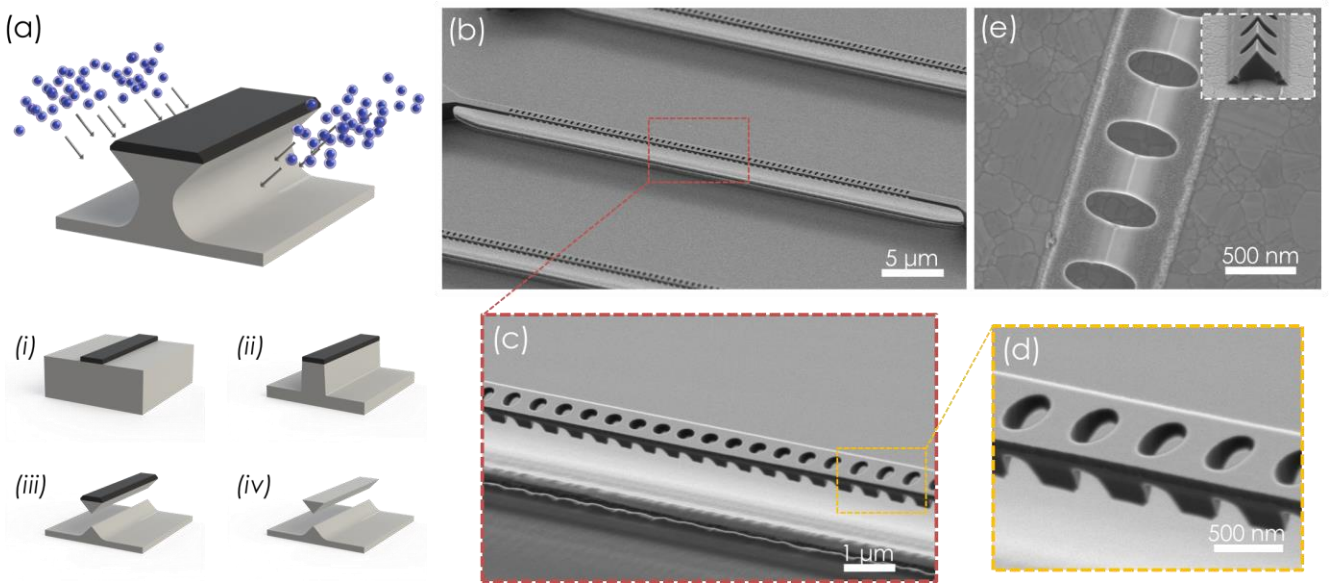

Figure 2 | Fabricated diamond optomechanical crystals. (a) Illustration of angled-etching used to realize diamond optomechanical crystals. Angled-etching nanofabrication steps: (i) define an etch mask on substrate via standard fabrication techniques, (ii) transfer etch mask pattern into the substrate by conventional top down plasma etching, (iii) employ angled-etching to realize suspended nanobeam structures (see illustration), (iv) remove residual etch mask. SEM images of **(b)** a fabricated diamond optomechanical crystal, **(c)** zoomed in view of the defect region, and **(d)** high-resolution image of fabricated air holes comprising the Bragg mirror region. **(e)** SEM image of an (inverted) diamond optomechanical crystal, liberated from the diamond substrate via stamping on a silver-coated silicon wafer. Inset shows a tilted (60°) SEM image of a broken diamond optomechanical crystal, revealing the triangular cross-section.

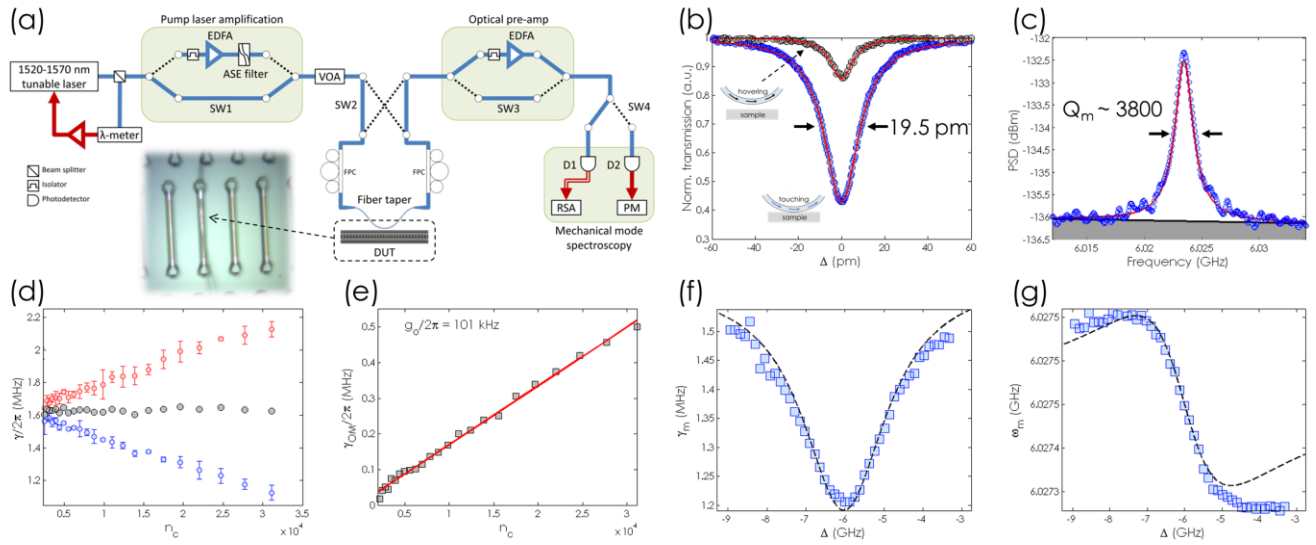

Figure 3 | Optical and mechanical mode spectroscopy. (a) Schematic of the fiber-optical set up for optical and mechanical mode spectroscopy (see *Methods* for description of symbols), with an optical micrograph of the dimpled fiber taper in contact with the diamond optomechanical crystal device under test. **(b)** Normalized optical transmission spectrum, centered at λ_o = 1532.4 nm ($\omega_o/2\pi$ = 196 THz), of a diamond optomechanical crystal measured with the dimpled fiber taper hovering (black circles) and touching (blue circles) the device, with corresponding Lorentzian fits indicated by solid red lines. With the dimpled fiber taper in contact with the device, the Lorentzian fit yields an optical linewidth of 19.5 pm and ~ 57% on-resonance transmission, corresponding to a measured total and intrinsic optical Q-factor of 7.85 x 10^4 and 1.20 x 10^5, respectively. **(c)** Optically transduced power spectral density of the fundamental 'flapping' mode at $\omega_m/2\pi$ = 6.023 GHz. Note, this mechanical spectrum was collected at low input laser powers and reveals the thermal Brownian motion of the cavity. The Lorentzian fit, indicated by the solid red curve, estimates a mechanical Q-factor of ~ 3800. **(d)** Measured mechanical linewidth (γ) collected at laser detuning of $\Delta = +\omega_m$ (red circles) and $\Delta = -\omega_m$ (blue circles). Black circles indicate the intrinsic mechanical linewidth values (γ_i) obtained by taking the average of the detuned data. An average value of $\gamma_i/2\pi$ = 1.63 +/- 0.012 MHz is estimated from the plot. **(e)** The optomechanically induced damping (γ_{OM}, black squares), calculated by subtracting γ_i from the blue-detuned mechanical linewidths, plotted versus intracavity photon number. A linear fit (red line) yields $g_o/2\pi$ = 101 kHz. The **(f)** optically amplified mechanical loss rate and **(g)** optical spring shifted mechanical frequency measured as a function of laser frequency blue detuned from the cavity, at an constant intercavity photon number of n_c = 2.5 x 10^4. Fits to **(f)** and **(g)** yield $\gamma_i/2\pi$ = 1.60 MHz and $g_o/2\pi$ = 102 kHz, consistent with values estimated from mechanical linewidths versus intercavity photon number.

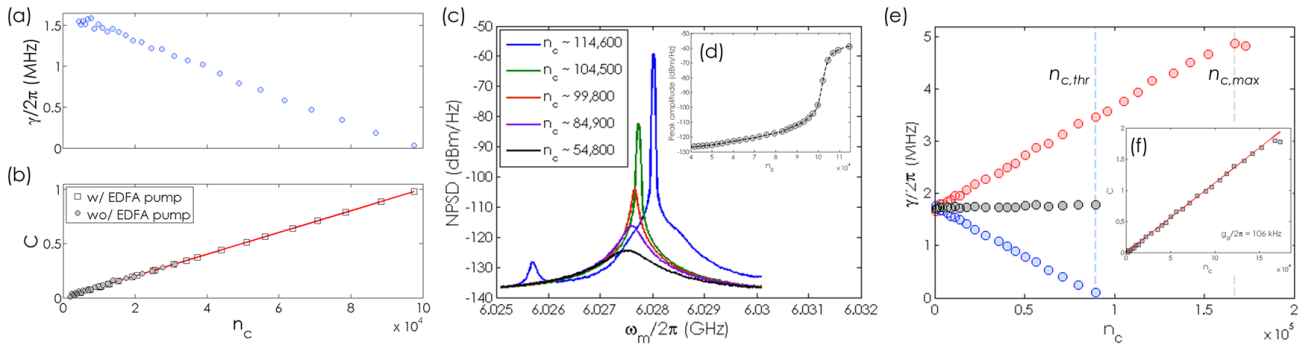

Figure 4 | High power optomechanical transduction and phonon lasing. (a) Measured mechanical linewidths and **(b)** corresponding cooperativity values collected with the amplified pump laser resonant with the blue detuned motional sideband ($\Delta = -\omega_m$), as a function of intracavity photon number (n_c). Data points collected with (open squares) and without (black circles) the amplified pump laser are included. Note, the cooperativity values measured without the amplified pump were calculated using γ_{OM} data plotted in Figure 3 (e), using the previously measured intrinsic mechanical linewidth, $\gamma_i/2\pi \sim 1.63$ MHz. **(c)** Noise power spectral densities (NSPD) collected below, at, and above the input power threshold for phonon lasing. The large shoulder feature and small satellite peak in the above-threshold mechanical spectrum correspond to beating of the phonon laser line with low-frequency modes of the nanobeam structure. The inset **(d)** plots the peak NSPD amplitude versus input optical power, indicating the intracavity photon threshold for phonon lasing is at $n_c \sim 10^5$. **(e)** Measured mechanical linewidths (γ) collected at laser detuning of $\Delta = +\omega_m$ (red circles) and $\Delta = -\omega_m$ (blue circles) as a function of input photon number for a second diamond optomechanical crystal device. Black circles indicate the intrinsic mechanical linewidth values (γ_i) obtained by taking the average of the detuned data, up to the phonon lasing threshold, $n_{c,thr}$ (indicated by the vertical blue dashed line). An average value of $\gamma_i/2\pi = 1.74$ MHz is estimated from the plot for this device. The onset of thermo-optically induced bistability shifts of the cavity resonance due to high intracavity photon population is indicated in **(f)** by the vertical grey dashed line. The inset shows the corresponding optomechanical cooperativity ($C = \gamma_{OM}/\gamma_i$, black squares) plotted versus intercavity photon number. A linear fit (red line) to the cooperativity values yields $g_o/2\pi = 106$ kHz for this device.

SUPPLEMENTARY INFORMATION

i) Guided acoustic phonon modes in angled-etched diamond optomechanical crystals

To supplement our discussion on the guided acoustic phonon modes of diamond optomechanical crystals (OMCs) fabricated by angled etching, we present normalized displacement profiles of the nominal unit cell at the Γ ($k_x = 0$) and X ($k_x = \pi/a$) of the mechanical bandstructure displayed in Figure 1 (c) of the main text. Figure S1 and S2 reveal the guided acoustic modes categorized by even (solid black lines) and odd (dashed blue lines) vector symmetries about the *y*-axis, respectively, with displacement profiles originating from the indicated band edges shown as insets (three dimensional, top down and cross-section views included). Note, the unit cell lattice constant in the displacement profiles is displayed between the ($h_{w,n}$, $h_{h,n}$) and ($h_{w,n+1}$, $h_{h,n+1}$) center points, in order to clearly reveal displacement components within the air holes. Mechanical simulations included here and throughout the main text use the full anisotropic elasticity matrix of diamond[1], where (C_{11}, C_{12}, C_{44}) = (1076, 125, 578) GPa. However, due to considerations expanded upon in later sections of *Supplementary Information*, devices characterized in this work were ultimately fabricated with their x-axis oriented with the in plane [110] crystallographic direction. Thus, a rotated version of anisotropic elasticity matrix ensured proper device orientation in our simulations, with guided mode propagation along the *x*-axis aligned with the [110] crystallographic direction, with the z-axis aligned with [001]. Only a small (< 10 %) change in the guide mode frequencies was observed between simulations with unit cell x-axis alignment to the [100] and [110] in plane crystal directions.

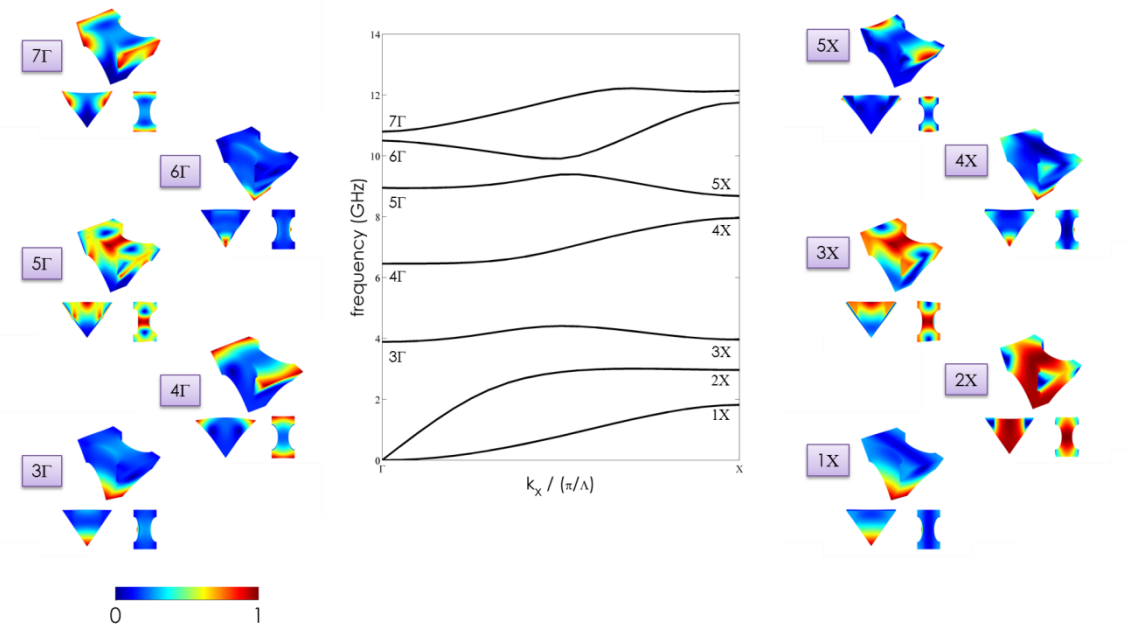

Figure S1. Acoustic guided modes with *y*-symmetric vector symmetries supported by angled-etch diamond OMCs. Normalized three-dimensional mechanical displacement profiles of the guided modes originating from the Γ-point and X-point are included as insets.

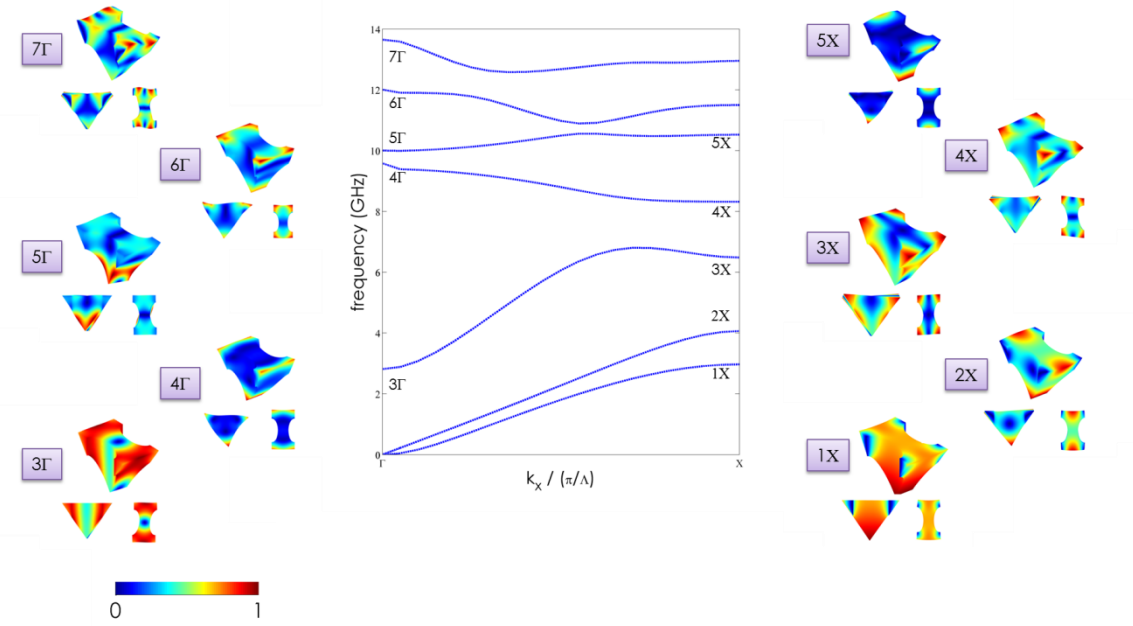

Figure S2 Acoustic guided modes with *y*-antisymmetric vector symmetries supported by angled-etch diamond OMCs. Normalized three-dimensional mechanical displacement profiles of the guided modes originating from the Γ-point and X-point are included as insets.

While the mechanical bandstructures reveal a rich library of guided acoustic modes in the few to 14 GHz frequency range, only guided modes originating from y-symmetric bands ultimately couple to the optical cavity[2]. Additionally, modes originating from the Γ-point ensure large optomechanical coupling rates in the final design[3]. With this in mind, two modes from the Γ-point of y-symmetric bands enable design of diamond OMCs with large single-photon optomechanical coupling rates, g_o. Specifically, the Γ-point modes from the 4th and 7th *y*-symmetric bands, referred to as the "flapping" and "breathing" modes, respectively, were both investigated. However, due to its higher guided mode frequency, fabricated structures based on designs optimized for the diamond OMC breathing mode were not ultimately studied in this work.

ii) Optimized diamond optomechanical crystal design

As discussed in the main text, the final diamond OMC design relies on transitioning from a "mirror" region formed by the base unit cell in Figure 1 (a) to a "defect" cell, which localizes the target optical and mechanical guided modes into their respective quasi-bandgaps. Out-of-plane scattering losses in the optical cavity were then minimized by transitioning from the mirror region to defect cell over seven lattice periods. This "defect region" is parameterized by the maximum change in lattice constant in the defect region, $d = (1 - a_{defect}/a_{nominal})$, the aspect ratio of the center hole, and curvature of the transition. Figure S3 illustrates the mirror to defect cell transition of our optimized diamond OMC design. The optimized design was determined via previously described numerical optimization methods[3], based upon finite element method (FEM) simulations (COMSOL) to calculate the optical and mechanical cavity resonance frequencies, ω_o and ω_m, the optical Q-factor, Q_o, and the single-photon optomechanical-coupling rate, g_o. In the optimization, the mirror region unit cell geometry (w, a, h_w, h_h) and the

aforementioned defect region parameters were varied, and a fitness function for the optimization was set such as to converge on a design with the largest g_o.

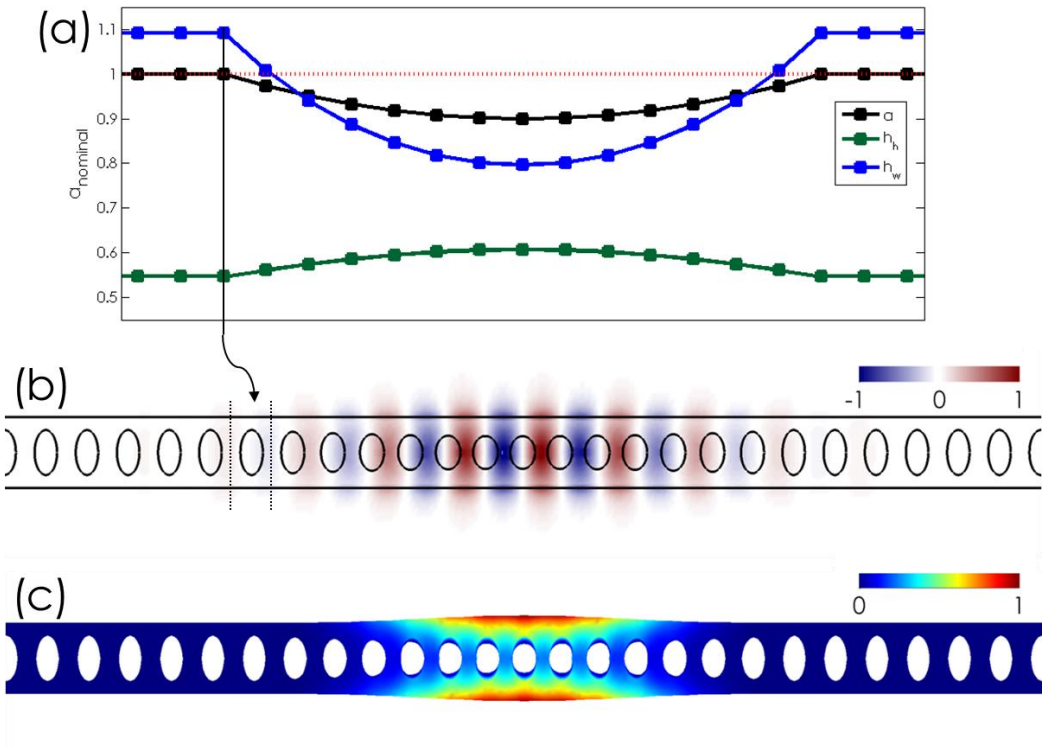

Figure S3 (a) Plot of the diamond optomechanical crystal defect region unit cell parameters along the length of the nanobeam, in units of $a_{nominal}$. Normalized **(b)** optical E_y field and **(c)** mechanical displacement profile of the optical and mechanical modes localized by the defect region.

iii) Calculation of single-photon optomechanical coupling rate

Both moving boundary ($g_{o,MB}$) and photo-elastic contributions ($g_{o,PE}$) to the single-photon optomechanical coupling rate were considered[3,4], with $g_{o,MB}$ given by:

$$g_{o,MB} = -\frac{\omega_o}{2}\frac{\oint(\mathbf{Q}\cdot\hat{\mathbf{n}})\left(\Delta\varepsilon\mathbf{E}_{\parallel}^2 - \Delta\varepsilon^{-1}\mathbf{D}_{\perp}^2\right)dS}{\int\varepsilon|\mathbf{E}|^2\,dV} \tag{S1}$$

where **Q** is the normalized displacement field, $\hat{\mathbf{n}}$ is the outward facing surface normal, **E** and **D** are the electric and displacement fields respectively, the subscripts ∥ and ⊥ subscripts designate field components parallel and perpendicular to the surface respectively, ε is the material permittivity, $\Delta\varepsilon = \varepsilon_{diamond} - \varepsilon_{air}$, and $\Delta\varepsilon^{-1} = \varepsilon_{diamond}^{-1} - \varepsilon_{air}^{-1}$. The photo-elastic contribution to the optomechanical coupling rate, $g_{o,PE}$, for a cubic crystal with *m3m* point symmetry and the x-axis and y-axis aligned to the [100] and [010] crystal directions, respectively, is given by:

$$\begin{aligned} g_{o,PE} = &-\frac{\omega_o\varepsilon_o n^4}{2}\frac{\int\sum\left(4\,\mathrm{Re}\left\{E_x^* E_y\right\}p_{44}S_{xy}\right)dV}{\int\varepsilon|\mathbf{E}|^2\,dV} \\ &-\frac{\omega_o\varepsilon_o n^4}{2}\frac{\int\sum\left(\left|E_x\right|^2\left(p_{11}S_{xx} + p_{12}\left(S_{yy}+S_{zz}\right)\right)\right)dV}{\int\varepsilon|\mathbf{E}|^2\,dV} \end{aligned} \tag{S2}$$

where Σ is a summation, according to Einstein notation x → y → z → x. S_{ij} are the stain tensor components, and p_{ij} are the photoelastic coefficients of diamond[5]: (p_{11}, p_{12}, p_{44}) = (-0.25, 0.043, -0.172).

As mentioned previously and in the main text, diamond OMCS were fabricated with their x-axis aligned with the [110] crystallographic direction. In the calculation of $g_{o,MB}$ this was taken into account by using a rotated version of the elasticity matrix[4]. To determine, $g_{o,PE}$, a rotated version of the photo-elastic tensor (p'_{ij}) was used, where:

$$p'_{11} = p'_{22} = \frac{1}{4}\left(p_{11}(3+\cos(4\theta)) + (p_{12}+2p_{44})(1-\cos(4\theta))\right) \tag{S3}$$

$$p'_{33} = p_{11} \tag{S4}$$

$$p'_{12} = p'_{21} = \frac{1}{4}\left(p_{12}\left(3+\cos(4\theta)\right)+\left(p_{11}-2p_{44}\right)\left(1-\cos(4\theta)\right)\right) \tag{S5}$$

$$p'_{13} = p'_{23} = p'_{31} = p'_{32} = p_{12} \tag{S6}$$

$$p'_{44} = p'_{55} = p_{44} \tag{S7}$$

$$p'_{66} = \frac{1}{4}\left(2p_{44}+\left(1+\cos(4\theta)\right)+\left(p_{11}-p_{12}\right)\left(1-\cos(4\theta)\right)\right) \tag{S8}$$

$$p'_{16} = p'_{61} = \frac{1}{4}\sin(4\theta)\left(2p_{44}+p_{12}-p_{11}\right) \tag{S9}$$

$$p'_{26} = p'_{62} = \frac{1}{4}\sin(4\theta)\left(p_{11}-p_{12}+2p_{44}\right) \tag{S10}$$

with $\theta = 45^{o}$. The final expression for $g_{o,PE}$ is then:

$$g_{o,PE} = -\frac{\omega_o \varepsilon_o n^4}{2} \frac{\int \begin{bmatrix} E_x^* & E_y^* & E_z^* \end{bmatrix} \begin{bmatrix} pS_1 & pS_6 & pS_5 \\ pS_6 & pS_2 & pS_4 \\ pS_5 & pS_4 & pS_3 \end{bmatrix} \begin{bmatrix} E_x \\ E_y \\ E_z \end{bmatrix} dV}{\int \varepsilon |\mathbf{E}|^2 dV} \tag{S11}$$

where:

$$\begin{bmatrix} pS_1 \\ pS_2 \\ pS_3 \\ pS_4 \\ pS_5 \\ pS_6 \end{bmatrix} = \begin{bmatrix} p'_{11} & p'_{12} & p'_{13} & 0 & 0 & p'_{16} \\ p'_{21} & p'_{22} & p'_{23} & 0 & 0 & p'_{26} \\ p'_{31} & p'_{32} & p'_{33} & 0 & 0 & 0 \\ 0 & 0 & 0 & p'_{44} & 0 & 0 \\ 0 & 0 & 0 & 0 & p'_{55} & 0 \\ p'_{61} & p'_{62} & 0 & 0 & 0 & p'_{66} \end{bmatrix} \begin{bmatrix} S_1 = S_{xx} \\ S_2 = S_{yy} \\ S_3 = S_{zz} \\ S_4 = 2S_{yz} \\ S_5 = 2S_{xz} \\ S_6 = 2S_{xy} \end{bmatrix} \tag{S12}$$

iv) Fabrication of diamond optomechanical crystals by angled-etching and analysis of cross-sectional symmetry

Our angled-etching approach[6,7], schematically depicted in Figures 2 (a) of the main text and Figure S4 (a), with corresponding SEM images displayed in Figure S4 subpanels (b) to (e), employs anisotropic oxygen-based plasma etching at an oblique angle to the substrate surface, resulting in suspended structures with triangular cross-section. Angled-etching is performed in a standard inductively coupled plasma-reactive ion etcher (ICP-RIE), however the diamond substrate is housed within a specifically designed aluminum Faraday cage which modifies the trajectory of the incident plasma ions towards the sample surface[7].

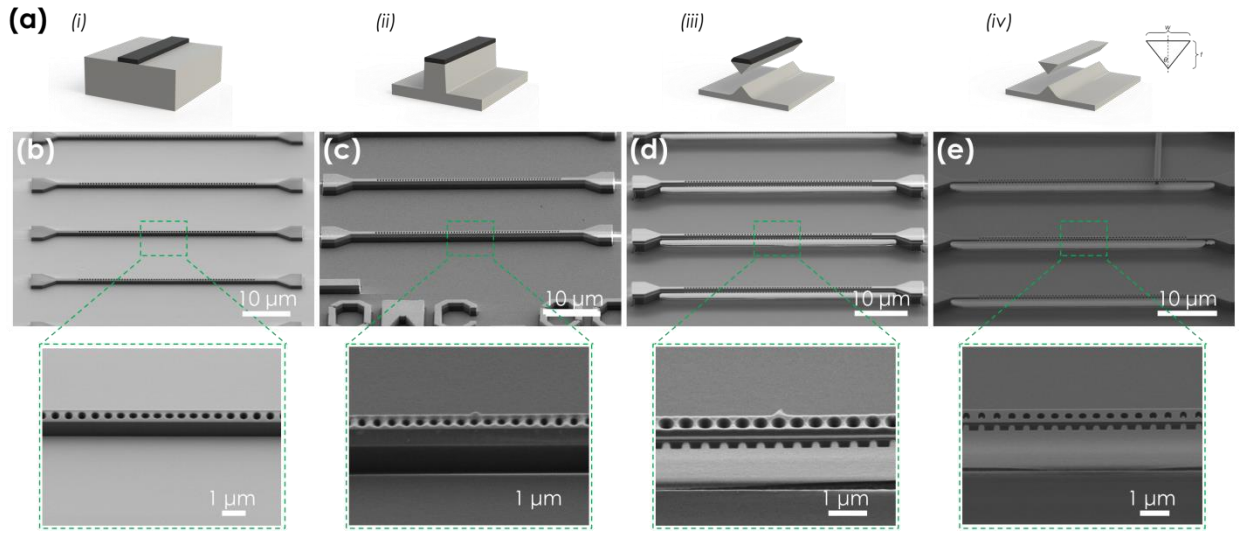

Figure S4 (a) Illustration of the angled-etching fabrication scheme used to realize free-standing structures in bulk single-crystal diamond. Angled-etching fabrication steps with corresponding SEM images: (i) define an etch mask on substrate via standard fabrication techniques (panel **(b)**), (ii) transfer etch mask pattern into the substrate by conventional top down plasma etching (panel **(c)**), (iii) employ angled-etching to realize suspended nanobeam structures (panel **(d)**), (iv) remove residual etch mask (panel **(e)**). All SEM images taken at a stage tilt of 60°.

Evidently, a unique consideration of angled-etched structures is their triangular cross-section symmetry. For instance, uneven sample mounting during the angled-etching step or diamond substrate wedge tolerances will lead to a distribution of effective etch angles across the sample, breaking symmetry in the final device cross-section[7]. Because of such asymmetry, localized mechanical and optical cavity modes will inevitably couple to anti-symmetric guided modes, which exist in their respective quasi-bandgaps, bringing about potentially significant loss. To circumvent this, periodic sample rotation was implemented during angled-etching to average the effective etch angle across the substrate.

We investigated this problem further by stamping angled-etch diamond optomechanical crystals onto a smooth silver-coated silicon wafer. High-resolution SEM images shown in Figure S5 (a) and (b), respectively, reveal diamond OMCs (oriented upside down) fabricated without and with sample rotation during angled-etching, with insets displaying a tilted cross-sectional view. Sample rotation appears to reduce the degree of asymmetry (defined as the offset in the bottom apex of the triangular cross-section from its centerline) considerably. However, even minimal asymmetry significantly reduces the simulated optical and mechanical Q-factors, as illustrate in Figure 2 (g) and (h) respectively, depending on the in-plane orientation of the device relative to the [100] crystal direction. Optical Q-factors of asymmetric diamond OMCs were performed by finite difference time domain (FDTD) simulations (Lumerical), while mechanical Q-factors were simulated by FEM simulations (COMSOL) using previously described techniques[2]. Interestingly, symmetry breaking in devices with their x-axis is oriented along the [110] crystal direction couple more weakly to guided modes of antisymmetric character, and thus, are likely more robust to fabrication imperfections (beyond cross-sectional asymmetry alone). Therefore, fabricated diamond optomechanical crystals characterized in this work were oriented along the [110] crystallographic direction.

Additionally, the high-resolution SEM image taken of diamond OMCs transferred onto silver substrates reveal an interesting bimodal character in the roughness on the angled-etched surfaces, with an extremely rough region localized to the upper portion of the angled-etch surface adjacent to the top side of the diamond nanobeam. In the lower portion of the angled-etched surfaces, a very smooth surface is apparent, and any roughness is not directly visible with the resolution of the SEM. This bimodal character in the surface roughness of the angled-etched sides is unique, and its origins are not presently understood. However, current knowledge suggests the greater degree of roughness near the upper half of the angled-etched surface results from micro-masking during fabrication.

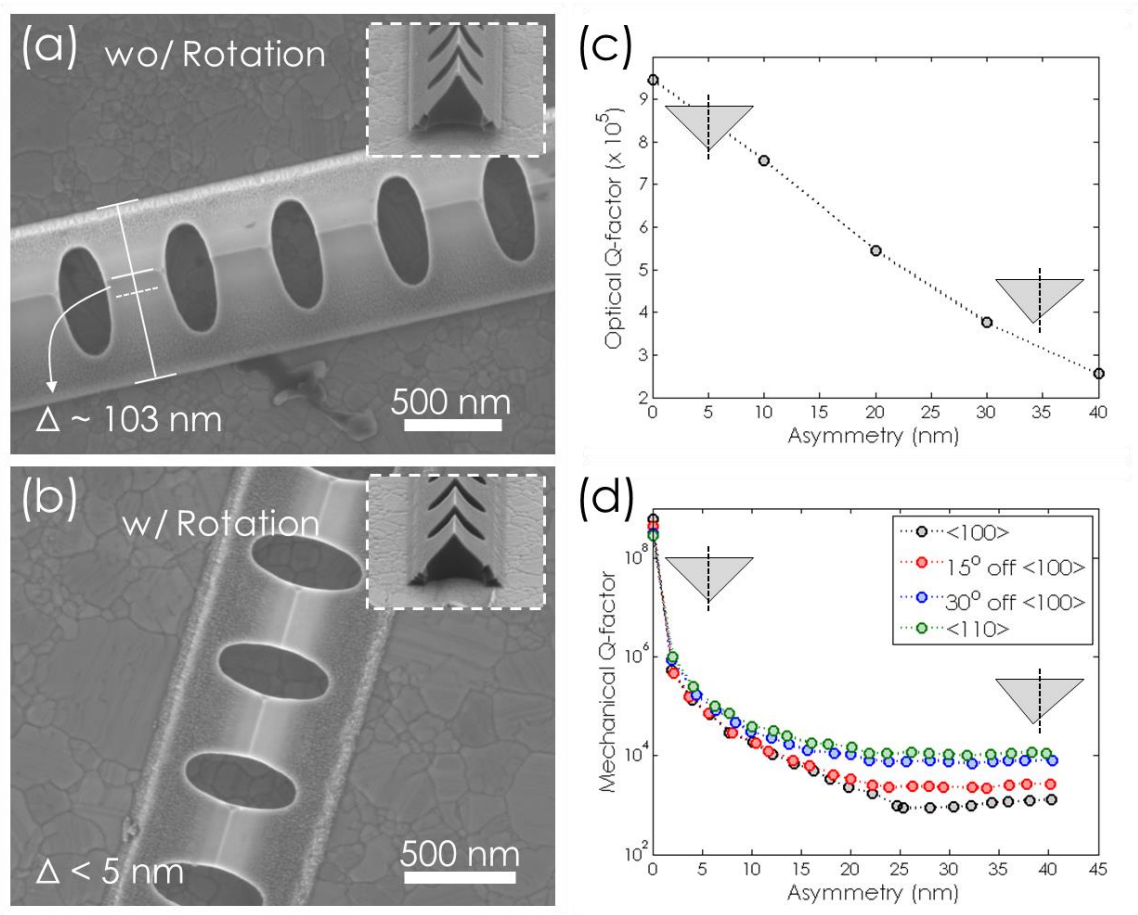

Figure 2 | Diamond optomechanical crystal fabrication symmetry. High resolution SEM images of the backside of diamond optomechanical crystals fabricated **(a)** without and **(b)** with sample rotation during angled-etching. A significant improvement in the cross-section asymmetry (Δ) is observed. Insets tilted SEM images of broken diamond nanobeams, revealing the diamond optomechanical crystal cross-section. The influence of cross-sectional asymmetry on the optical and mechanical Q-factors (as a function of in-plane nanobeam orientation with

the major crystallographic directions) is plotted in **(c)** and **(d)** respectively. Optical Q-factor simulations were performed using finite difference time domain (FDTD) simulations (Lumerical), while mechanical Q-factor simulations were performed by finite element method (COMSOL) using previously described techniques[2].

SUPPLEMENTARY REFERENCES

1 Klein, C. A. & Cardinale, G. F. Young's modulus and Poisson's ratio of CVD diamond. *Diamond and Related Materials* **2**, 918-923 (1993).

2 Eichenfield, M., Chan, J., Safavi-Naeini, A. H., Vahala, K. J. & Painter, O. Modeling dispersive coupling and losses of localized optical andmechanical modes in optomechanicalcrystals. *Opt. Express* **17**, 20078-20098 (2009).

3 Chan, J., Safavi-Naeini, A. H., Hill, J. T., Meenehan, S. & Painter, O. Optimized optomechanical crystal cavity with acoustic radiation shield. *Applied Physics Letters* **101**, 081115 (2012).

4 Balram, K. C., Davanço, M., Lim, J. Y., Song, J. D. & Srinivasan, K. Moving boundary and photoelastic coupling in GaAs optomechanical resonators. *Optica* **1**, 414-420 (2014).

5 Lang, A. R. The strain-optical constants of diamond: A brief history of measurements. *Diamond and Related Materials* **18**, 1-5 (2009).

6 Burek, M. J. *et al.* High quality-factor optical nanocavities in bulk single-crystal diamond. *Nat Commun* **5** (2014).

7 Burek, M. J. *et al.* Free-Standing Mechanical and Photonic Nanostructures in Single-Crystal Diamond. *Nano Letters* **12**, 6084-6089 (2012).